# JACS

# Broadband Ultrafast Photoluminescence Spectroscopy Resolves Charge Photogeneration via Delocalized Hot Excitons in Polymer:Fullerene Photovoltaic Blends

Kai Chen,[†,‡] Alex J. Barker,[†,‡] Matthew E. Reish,[†,§] Keith C. Gordon,[†,§] and Justin M. Hodgkiss*,[†,‡]

[†]The MacDiarmid Institute for Advanced Materials and Nanotechnology, New Zealand

[‡]School of Chemical and Physical Sciences, Victoria University of Wellington, Wellington 6140, New Zealand

[§]Department of Chemistry, University of Otago, Dunedin 9054, New Zealand

**S** *Supporting Information*

**ABSTRACT:** Conventional descriptions of excitons in semiconducting polymers do not account for several important observations in polymer:fullerene photovoltaic blends, including the ultrafast time scale of charge photogeneration in phase separated blends and the intermediate role of delocalized charge transfer states. We investigate the nature of excitons in thin films of polymers and polymer:fullerene blends by using broadband ultrafast photoluminescence spectroscopy. Our technique enables us to resolve energetic relaxation, as well as the volume of excitons and population dynamics on ultrafast



time scales. We resolve substantial high-energy emission from hot excitons prior to energetic relaxation, which occurs predominantly on a subpicosecond time scale. Consistent with quantum chemical calculations, ultrafast annihilation measurements show that excitons initially extend along a substantial chain length prior to localization induced by structural relaxation. Moreover, we see that hot excitons are initially highly mobile and the subsequent rapid decay in mobility is correlated with energetic relaxation. The relevance of these measurements to charge photogeneration is confirmed by our measurements in blends. We find that charge photogeneration occurs predominately via these delocalized hot exciton states in competition with relaxation and independently of temperature. As well as accounting for the ultrafast time scale of charge generation across large polymer phases, delocalized hot excitons may also account for the crucial requirement that primary charge pairs are well separated in efficient organic photovoltaic blends.
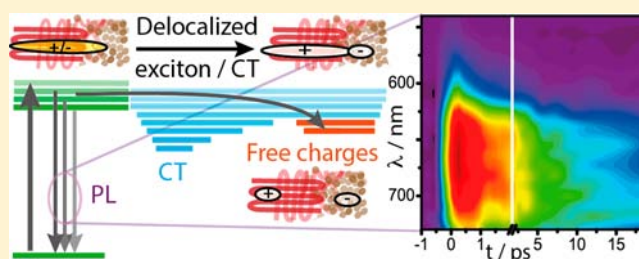
## INTRODUCTION

The nature of primary excitations in organic photovoltaic (OPV) blends is receiving renewed attention because of their importance to resolving questions raised by several recent developments. First, the observation of free charge carrier generation on ultrafast time scales in fullerene blends appears incommensurate with diffusion of excitons across polymer domains. Applying exciton diffusion coefficients measured on picosecond−nanosecond time scales $(1.8 \times 10^{-3}\ \mathrm{cm^2\ s^{-1}})$[1] would result in only ~0.3 nm exciton displacement within 100 fs (assuming 3-dimensional diffusion), whereas significant populations of free charge carriers are found to be already generated on this time scale in blends with ~10 nm polymer domain sizes.[2−7] Second, charges can be photogenerated in polymer films on an ultrafast time scale without the presence of donor/acceptor interfaces to separate excitons.[8,9] Third, recent spectroscopic and theoretical investigations of photocurrent generation in OPV blends have created an emerging view that free charge carrier photogeneration is mediated by short-lived delocalized states;[10−12] while it is generally accepted that delocalization within a manifold of interfacial charge transfer states provides the means to overcome the Coulomb binding

energy of charge pairs, it is reasonable to hypothesize that delocalized charge transfer states may be formed through coupling to delocalized excitons on an ultrafast time scale.

Optical spectroscopy, in particular photoluminescence (PL) spectroscopy, has contributed to an understanding of excitons in semiconducting polymers that can be summarized as follows in the context of OPVs: PL spectra present a significant Stokes shift as well as spectral narrowing and often stronger vibronic structure compared with absorption spectra. These observations, along with relatively high radiative relaxation rates, reflect a strong exciton binding energy $(\gg k_\mathrm{B}T)$, significant structural relaxation, and the propensity of excitons to be funneled to a small fraction of low energy states within their lifetime. Thus, strong binding necessitates incorporating charge-separating interfaces, while exciton mobility ensures that they diffuse to interfaces, which must therefore be distributed within the inherent range of exciton diffusion.

This simplistic model has subsequently evolved through the application of better ultrafast spectroscopic tools.[13] Polarization

resolved ultrafast PL spectroscopy reveals substantial loss of polarization anisotropy on sub-100 fs time scales.[14−16] These observations provoked the suggestion that a primary excitation initially spans a distribution of polymer chain orientations and rapidly loses anisotropy as it localizes on one subunit. Polarization anisotropy was also used to report on quantum coherence effects observed at room temperature in films of conjugated polymers. By applying two-time anisotropy decay spectroscopy, Collini et al. found that exciton motion on early time scales could be explained by relatively long-lived coherences between conformational subunits in an intermediate coupling regime.[17] More recently, Banerji et al. have resolved multiphasic PL spectral relaxation via ultrafast femtosecond upconversion spectroscopy, leading to the suggestion that exciton relaxation is actually slower than previously supposed and therefore can be circumvented by charge photogeneration in efficient OPV blends.[18−20] Accordingly, theoretical attention is now focused on developing a description of the structure and dynamics of excitons that are considerably more spatially extended than traditional conformationally defined spectroscopic units.[21,22] Kaake et al. have recently proposed that significant delocalization is a consequence of the uncertainty principle applied to ultrafast time scales.[23]

The clear implications of these findings for photocurrent generation in OPV blends motivated us to devise experiments that can resolve the volume and mobility of primary excitations on the time scale of charge photogeneration. Additionally, we sought to directly resolve the kinetic competition between exciton relaxation and charge photogeneration by measuring population decay and energetic relaxation in both polymer films and polymer:fullerene blends. Using a PL spectrometer with an ultrafast broadband Kerr gate shutter and resolving ultrafast annihilation at high excitation density, we are able to measure the volume of primary excitations. We find that primary excitations sample a substantial volume on ultrafast time scales and the sampled volume subsequently grows slowly as excitons relax within the first picosecond. We show that most charges are generated significantly faster than exciton relaxation, which can be clearly ascertained by comparing initial PL amplitudes and resolving the time-dependent Stokes shift. These results, supported by electronic structure calculations, suggest that free charge photogeneration is linked to highly delocalized hot excitons that couple to charge-separating interfaces.

## ■ EXPERIMENTAL DETAILS

**Materials.** Regioregular poly(3-hexylthiophene) (RR-P3HT) was purchased from American Dye Source, Inc. (ADS306PT), and phenyl-$C_{61}$-butyric acid methyl ester (PCBM) was purchased from Sigma-Aldrich. Thin films were spin-cast from chloroform solutions of P3HT (7.5 mg/mL) and P3HT:PCBM (1:1 by weight, 15 mg/mL) at 2500 rpm on clean fluorescence-free fused silica substrates. Samples are sealed inside a cell in a nitrogen glovebox. In the case of annealed films, the sample was annealed at 140 °C for 10 min in nitrogen environment. The film thicknesses were measured by a surface profiler (Dektak, Veeco) to be 70 nm for pristine P3HT and 100 nm for the P3HT:PCBM blends. The peak absorption values were OD 0.35 at 550 nm for the annealed P3HT, OD 0.31 at 510 nm for annealed P3HT:PCBM and OD 0.25 at 480 nm for unannealed P3HT:PCBM. We also repeated measurements on devices in order to verify the relevance of the measured photophysics to efficient devices. In this case, we used P3HT:PCBM blend devices cast from chlorobenzene and fabricated in a glovebox according to reference.[24]

**Ultrafast Broadband PL Spectroscopy.** Our ultrafast PL spectrometer is based on the optical Kerr shutter depicted in Figure

1a.[25−27] The system is driven by a Ti-sapphire amplifier (Spitfire, Spectra-physics, 100 fs pulse duration, 800 nm, 3 kHz). A portion of
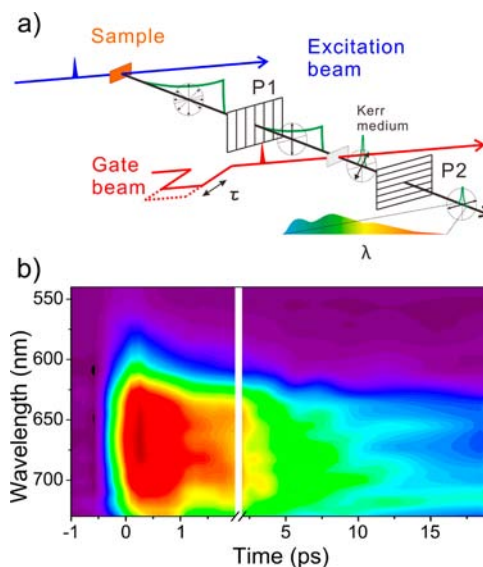


**Figure 1.** (a) Experimental setup for ultrafast PL spectroscopy via Kerr gating. (b) Time-resolved PL spectra for a thin film of RR-P3HT following 480 nm excitation (2 $\mu$J/cm$^2$).

the output of the amplifier pumps an optical parametric amplifier (TOPAS) as the tunable excitation source. The excitation intensity is kept <5 $\mu$J/cm$^2$ except where noted in the excitation intensity dependence measurements. PL emission is collected by a pair of off-axis parabolic mirrors to the Kerr shutter. Two wire grid polarizers (PFU04C, Moxtek) P1 and P2 are used to provide broadband transmission, high contrast and low dispersion. The intense 800 nm pulse (gate pulse) induces transient birefringence in the Kerr medium which is placed between P1 and P2 to open the shutter. For optimum gate efficiency, the polarization of the gate pulse is rotated 45° with respect to the first polarizer, and a pulse energy of ∼50 $\mu$J is focused to a 500 $\mu$m spot overlapping with the collected PL signal, which is focused to 100 $\mu$m in the Kerr medium. The gate timing is adjusted by varying the optical delay between the excitation and gate pulse. The pulse energy of our system is sufficient to employ fused silica (Spectrosil B, 1 mm thickness) as the Kerr medium and thereby achieve a Kerr efficiency of ∼8% while maintaining a low background and minimize dispersion. The broadband phase matching condition for the Kerr effect enables us to take broadband spectra without changing the alignment. A long pass and a short pass filter are used to block the scattering of excitation and gate beams. The gated PL was then measured by a polychromator (SP2300, Princeton Instruments) with an intensified CCD camera (PIMAX3, Princeton Instruments). A single spectrum accumulates 30000 shots with the iCCD camera in gating mode. Each single spectrum is background corrected by subtracting the spectrum at negative time and corrected by the wavelength dependent Kerr gating efficiency and detector sensitivity. To check that the same alignment is maintained for different samples, position detectors are used to monitor both excitation beam pointing and PL emission collection. Unless otherwise stated, the excitation polarization was set to the magic angle with respect to the first polarizer in the Kerr shutter. The time resolution of the TRPL system is ∼200 fs (ascertained from the fwhm of the scattering excitation pulse), which is further improved via deconvolution. The useful bandwidth is from 420 to 730 nm when using 800 nm gate pulses. We were able to verify that our measurements were not affected by degradation during the measurement by checking that the PL intensities (both gated and ungated) before and after the measurement and at specified excitation densities had not significantly changed.

**Transient Absorption (TA) Spectroscopy.** TA measurements were performed using the Ti-sapphire amplifier described in the PL spectroscopy section above. A small fraction of the fundamental light (800 nm) was used to probe the photoinduced absorption associated with the presence of both bound and free charge pairs in P3HT:PCBM blends.[3] After transmission through the sample, the probe light was dispersed on to a linear photodiode array, which was read out at 3 kHz. The differential transmission signal ($\Delta T/T$) is calculated according to sequential probe shots corresponding to pump on vs off, where the excitation rep-rate is 1.5 kHz.

For charge generation TA measurements, an optical parametric amplifier (TOPAS) provided 100 fs excitation pulses at 480 nm, which were chopped at 1.5 kHz. Excitation intensity at the sample was kept at 7 $\mu$J/cm$^2$. The relative delay between pump and probe pulses (up to 3 ns) was varied using a broadband retroreflector mounted on an automated delay stage. For charge recombination TA measurements, excitation light was provided by a Q-switched Nd:YVO$_4$ laser (AOT-YVO-25QSP) generating 700 ps pulses at 532 nm. The pump–probe delay was electronically varied (ns–ms) by a delay generator (Stanford Research Systems DG535). Excitation density was varied as indicated in the figures, and fits were carried out as described in reference 3. All samples were measured under dynamic vacuum and, where indicated, cooled to 10 K by a closed-cycle helium cryostat.

**Electronic Structure Calculations.** Density functional theory (DFT) calculations were performed using the Gaussian 09 software package.[28] For all calculations, the 6-31G(d) basis set was employed. All calculations used either the B3LYP or CAM-B3LYP[29] functionals, and for CAM-B3LYP calculations, the Gaussian 09 default values for initial HF exchange ($\alpha$), final HF exchange ($\beta$) and the range separation parameter ($\mu$) were employed. For all calculations, environmental effects have been neglected as it has been shown previously that a solvent field has only minor effects on the properties of neutral states in oligomer calculations.[30,31] Natural transition orbitals (NTOs) were generated for the lowest energy transitions using Gaussian 09 and population analysis of the NTOs was assisted by the Multiwfn program.[32]

## ■ RESULTS AND DISCUSSION

Our experimental setup, depicted in Figure 1a and described in the Experimental Details section, offers several key benefits. In addition to broadband ultrafast detection and sufficient sensitivity to measure in the linear excitation regime, we benefit from the ability to resolve *time-integrated* spectra under identical conditions simply by removing one of the polarizers of the Kerr shutter. A further key advantage of our experimental setup is that having optimized the alignment, we are able to account for and reproduce absolute PL intensities. No further changes are required when samples are changed, thereby positioning us to reliably compare not only PL dynamics but also amplitudes for different samples.

**PL Dynamics in Neat Films.** To understand the role of emissive excitons in polymer/fullerene blends, we first investigated the intrinsic PL dynamics in P3HT thin films. Figure 1b shows the broadband PL decay of a film of RR-P3HT following 480-nm excitation. The broad PL spectrum in Figure 1b is clearly seen to undergo narrowing and red-shifting on subpicosecond time scale. We can further explore these effects by deconstructing into constituent spectral slices and kinetic traces.

Figure 2a shows the normalized PL spectra of RR-P3HT at early (200 fs) and later (2−10 ps) delay times, in addition to the time-integrated spectrum. Both of the time-resolved spectra exhibit substantial higher energy PL than the time-integrated spectrum. By 10 ps, the PL edge approaches that for the time-integrated spectrum; however, the 200-fs PL spectrum has considerably more intensity at higher energy. This high-energy
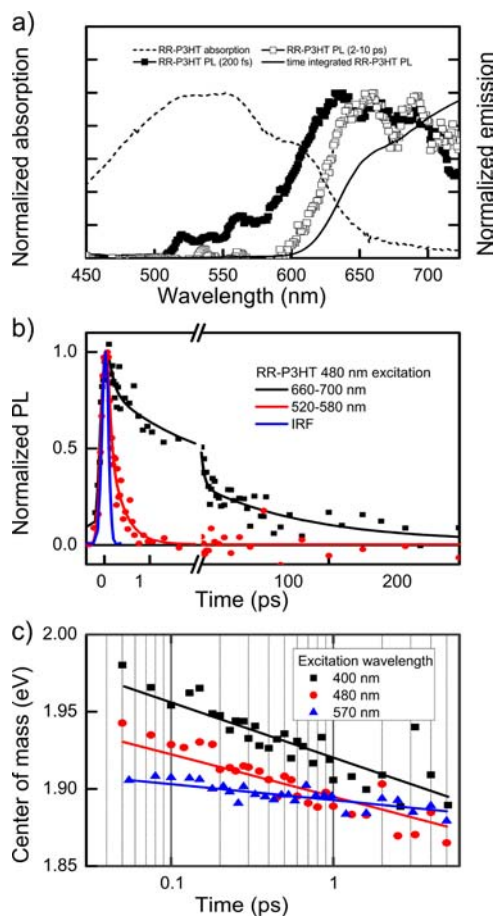


**Figure 2.** (a) Absorption spectra and PL spectra at various times for a thin film of RR-P3HT following 480 nm excitation (4 $\mu$J/cm$^2$). (b) PL decay kinetics for RR-P3HT after 480 nm excitation (2 $\mu$J/cm$^2$) in different spectral windows. Fitting parameters are provided in Table 1. (c) Time-dependent spectral center of mass for a thin film of RR-P3HT following excitation at various wavelengths. These plots all overestimate the absolute center of mass because the optical filter for the gate beam also removes PL beyond 720 nm.

phase of PL has not previously been observed for RR-P3HT, perhaps because previous ultrafast PL measurements were undertaken using upconversion spectroscopy where specific wavelengths must be targeted, usually guided by the steady state PL spectrum.[19,33,34] The fact that the high energy PL phase overlaps substantially with the absorption spectrum highlights the degree to which we are resolving PL from nonthermalized ('hot') states in the process of relaxing either structurally or via transfer to the lower energy sites available in a semicrystalline film. We can quantify the energetic relaxation in the excited state manifold via the high-energy edge of the PL spectra. At ~200 fs, the PL edge (~500 nm) is 0.1 eV lower than the photoexcitation energy and decays to 0.5 eV within 1 ps, corresponding to a PL edge of 600 nm. When repeating with 570 nm excitation, which selectively excites semicrystalline polymer phases and reduces the energetic contribution of static disorder (Supporting Information), we find that the PL edge at 600 nm is initially also only 0.1 eV lower than the excitation energy at ~100 fs, thereby confirming that excitations cannot be regarded as relaxed on this time scale. The lack of suitably sharp optical filters prevented us from repeating the experiment with even lower excitation energy to further refine the lower limit of the Stokes shift.

To probe the effect of static disorder, we also measured the absorption and ultrafast PL spectra for regiorandom (RRa-P3HT), whose random side chain placement suppresses the formation of crystalline lamellae in favor of a more amorphous morphology. The stronger dynamic red-shift observed for RRa-P3HT (Supporting Information) highlights the role of static disorder in explaining the energetic relaxation beyond the first 200 fs.

Figure 2b shows PL kinetics for the high- and low energy ranges of the same RR-P3HT data described above. The short-lived ∼100 fs presence of the high energy PL confirms why it is not observed in time-integrated measurements. The main PL feature (660−700 nm) exhibits a multiexponential decay characterized by components on ∼100 fs, 1.2 ps, and 40 ps time scales. We verified that these dynamics are not affected by bimolecular interactions by measuring the intensity dependence of time-integrated PL intensities (which are sensitive to sublinearity on any time scale) and observing that the sublinearity threshold occurs at 4-fold higher excitation densities than we used to obtain the time-resolved data. The ∼100 fs decay component has been observed in some studies[33] but not others,[19,34] and only for thin films, suggesting that its presence is sample dependent and may be attributed to quenching by intrinsically doped charges, aggregates or conformational defects. Other studies have resolved similar lifetimes as our picosecond components, but generally also observe a longer component of ∼500 ps.[19] The absence of a long component in our data could be for two reasons: (i) the longest lifetime is shortened in the presence of defects (e.g., intrinsically doped charges),[35] and (ii) the Kerr gate technique is not well suited for resolving slower dynamics because the leakage background begins to overwhelm the gated signal at the same wavelength. Nevertheless, we focus here on the ultrafast to early picosecond dynamics, which we confirm accounts for charge photogeneration processes.

We can further apply analysis to our broadband data set that captures the dynamics of energetic relaxation within a disordered film. According to the description of relaxation via diffusion within an inhomogenously broadened Gaussian density of states introduced by Kersting et al., spectral relaxation is expected to follow a logarithmic decay.[36,37] Figure 2c confirms that the spectral center of mass undergoes a logarithmic decay within the first 10 ps, with a greater amplitude observed upon exciting higher into the density of states. A corollary of this analysis is that the exciton diffusion coefficient undergoes a similar decay over time and is enhanced by energetic bias mostly within the first picosecond.[38]

The small initial Stokes shift and subsequent ultrafast spectral relaxation suggest that we are capturing a nonrelaxed and possibly more delocalized excitation on the ∼100 fs time scale. This assertion is supported by considering the time scales of nuclear modes that strongly couple to the excitation and drive exciton localization; the C=C stretching mode at ∼1450 cm$^{-1}$ has a period of 23 fs and may establish a new configuration of bond-lengths within a couple of periods, while the softer torsion modes at ∼200 cm$^{-1}$ have a period on the order of 170 fs and therefore take longer to establish the final structure of a relaxed localized exciton. Time-resolved vibrational spectroscopy measurements in solution suggest that structural reorganization extends well into the picosecond regime.[39] With this in mind, we undertook to measure the initial volume of the hot excitons prior to relaxation.

**Measurement of Excitation Volume.** Our approach to measuring the initial excitation volume is to induce ultrafast quenching and observe the reduction in ultrafast PL intensity. We can then apply the Perrin equation for quenching of the initial PL amplitude as a function of excitation volume:[40]

$$\frac{I}{I_0} = e^{-cV} \qquad (1)$$

According to the Perrin equation (eq 1), the relative PL amplitude $(I/I_0)$ is related to the probability that a quencher falls within the quenching volume $(V)$. By expressing that probability in terms of Poisson statistics for a given homogeneous quencher concentration $(c)$, and assuming that excitations are completely quenched if there is a quencher within their volume, one can obtain the quenching volume from the concentration dependence of static quenching, referring to quenching of the initial amplitude. Due to the heterogeneous distribution of PCBM quenchers in phase separated blend films, we instead investigated quenching via annihilation reactions in neat films of RR-P3HT. Similar to previous studies that induce annihilation to measure exciton diffusion,[1,35] we are able to control the quencher concentration via the excitation intensity; however, we are most interested in ultrafast time scales. By monitoring variation of the peak PL intensity when the Kerr shutter is centered at 100 fs, we are able to ascertain the quasi-instantaneous excitation volume. Importantly, the measurement reveals an exciton volume that is independent of any assumptions about its shape, which is clearly highly anisotropic in polymer films. Long-range resonant energy transfer between excitons is too slow to account for quenching of the ultrafast amplitude; therefore, we consider annihilation to be underpinned by tunneling exchange interactions of the excited electrons. We reformulated the Perrin equation to account for the Gaussian spatial distribution of excitation densities within the excitation beam, yielding the following equation, where $c$ is related to the excitation intensity, as is further explained in the Supporting Information:

$$\frac{I}{I_0} = (1 - e^{-cV})/cV \qquad (2)$$

Figure 3a shows the intensity dependence of initial PL amplitudes for RR-P3HT films as a function of excitation density. Increasing excitation densities are found to induce substantial quenching of the initial PL amplitude. The intensity dependent curve is well fit by eq 2, resulting in an effective initial excitation volume of 17 nm$^3$. This volume corresponds to an effective radius of 1.6 nm; however, if the excitations are assumed to have a more elongated shape, they must have a significant length (e.g., for a cylinder with radius of 0.8 nm based on twice the interchain distance, corresponding excitation length is ∼9 nm). Thus, we find that excitations initially sample a remarkably large volume within their first 100 fs. Moreover, this value must be considered a lower bound on the initial quenching volume because (i) excitations are likely to already be localizing on the time scale of the excitation pulse, and (ii) deviation from the assumption of complete quenching within the excitation volume would lead to underestimation.

Although we do not directly resolve the time scale of annihilation quenching, the degree of static quenching enables us to place an upper bound on the time constant. If we assume that with infinitely fast time resolution the initial PL amplitudes should be independent of intensity, we can then artificially add
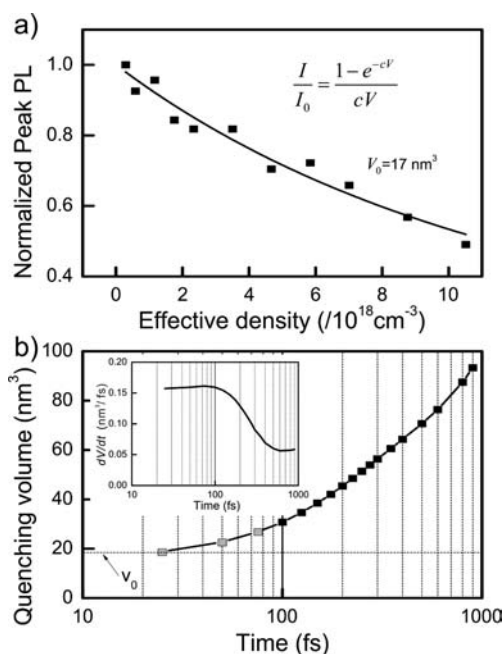
**Figure 3.** (a) Effective excitation density dependent peak PL intensities for a thin film of RR-P3HT excited at 480 nm and corresponding fit according to eq 2. Peak PL intensities are integrated across the spectrum at the peak of the IRF and normalized by the low-fluence PL intensity scaled by the excitation density (noting that the excitations added as quenchers are themselves emissive). (b) Time-dependent integrated excitation volume obtained by applying eq 2 to time-dependent fits of PL decay at increasing excitation densities following 480 nm excitation for a thin film of RR-P3HT. The differential form of the data is shown in the inset.

a component to the fitted data with a substantially faster time constant, reconvolute with the IRF, and observe the effect on the apparent static quenching. We require the unresolved quenching component to be faster than 45 fs in order to account for the observed 50% static quenching at high excitation density. Thus, the large excitation volume measured applies to the ultrafast time scale on which the exciton relaxation occurs. While others have used ultrafast annihilation to estimate excitation radii of ~3−7 nm for P3HT[41] and 5 nm for MEH-PPV[42] via the density threshold using TA spectroscopy, our detection and Perrin analysis provides the most direct measurement of initial excitation volumes. Our excitation volume would be 10-fold overestimated at >150 nm$^3$ if our analysis were based simply on the sublinearity threshold and assuming a uniform excitation density. The reliability of our analysis is aided by the fact that ultrafast PL signals isolate the behavior of the primary excitation of interest, rather than including charges, and other artifacts like electroabsorption and thermally modulated absorption encountered in TA spectroscopy at high excitation densities.[43]

We can extend our excitation intensity dependent PL measurements beyond the initial excitation time scale and apply the Perrin model to time resolve the integrated volume sampled by excitations. Here, the time-dependent volume (i.e., the total volume sampled up to a certain time, rather than the instantaneous volume at a certain time) is obtained by fitting the excitation density dependent PL intensities to eq 2 for each time. Figure 3b shows that the integrated excitation volume grows, but as seen in the differential form of the data in the inset, the rate of growth decays substantially within the first

picosecond. The integrated volume obeys a logarithmic growth, thus invoking a diffusion coefficient that is exponentially decaying over this time scale. We are unable to fit PL decays with a time-independent bimolecular rate constant, as others have for exciton annihilation studies in P3HT over longer time scales (10's to 100's of ps).[1] The logarithmic growth in excitation volume is strongly correlated with the spectral relaxation in Figure 2c. From this correlation, we can conclude that excitations have strongly enhanced mobility during the early time scale that they are energetically relaxing. Therefore, the spectral relaxation cannot be explained by structural relaxation alone, but there must be a strong component of energetically biased diffusion.[44] The rapid motion we observe on ultrafast time scales has an interesting implication; by initially moving on a competitive time scale with the lattice response time (which may be limited by the torsion time scale of ~170 fs), the excitation is able to rapidly sample a large volume in a partially bound state. As we will discuss later, this observation is highly relevant to charge photogeneration, which happens predominantly on the subpicosecond time scale.

Our time-resolved measurements of integrated volume cannot directly determine whether the initial excitation maintains its size or localizes somewhat upon diffusing since the total volume sampled is the integral of instantaneous volume over the path length. Any localization of the instantaneous (coherent) volume can be offset by an increase in the diffusive (incoherent) volume. However, the observation of ultrafast polarization anisotropy loss provides an indication that the initial excitation rapidly localizes. Consistent with others,[15,17,19] we measure initial polarization anisotropy values of ~0.2 (Supporting Information) within our time resolution. The ultrafast decay from the theoretical value of 0.4 for parallel absorption and emission transition dipole moments is evidence for ultrafast reorientation from the initially excited state as it localizes from an initially delocalized excitation that spans a distribution of polymer chain orientations.[15−17,19] Interestingly, we observe slightly less polarization anisotropy loss when preferentially exciting semicrystalline phases at 570 nm. This can be understood by the greater orientational order in semicrystalline phases, which restricts depolarization even from very delocalized excitations. This observation highlights the advantage of our method that directly measures excitation volume.

**Electronic Structure Calculations.** To better understand our quasi-instantaneous excitation volume measurements in the framework of electronic states, we undertook electronic structure calculations on model polythiophene oligomers where the hexyl side chains were replaced with methyl groups for computational expediency. To attain a structure with accurate electronic characteristics, we calculated oligomer geometries using the B3LYP and long-range corrected CAM-B3LYP functionals for both full geometry optimizations and optimizations constrained to the $C_s$ point group (mirror symmetry). It should be noted that in order to complete calculations on chains with sufficient length and at a level of theory which deals effectively with electron correlation, calculations were done using isolated chains. In thin-films, a lamellar arrangement is generated with some degree of interchain coupling and induced planarity that our calculations do not account for.[45,46] The inverse of repeat unit $(1/n)$ dependence of the TD-DFT excitation between 4 and 32 monomer units for each calculation method is shown in figure 4a. These data indicate that the best match with the
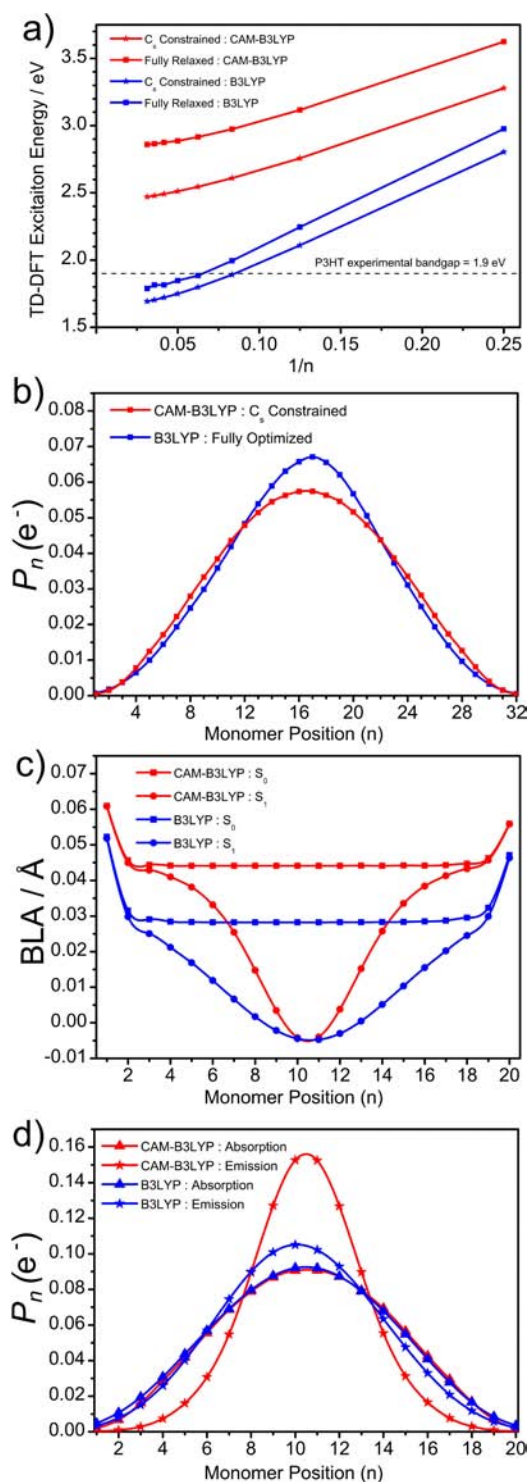
**Figure 4.** (a) The length dependence of TD-DFT excitation energy using the B3LYP and CAM-B3LYP functionals as well as constrained and unconstrained geometries. (b) Excited electron probability per monomer unit vs monomer position for the two methods that give the closest match to the experimental excitation energy. (c) BLA in the optimized ground and excited state 20-unit oligomers using the B3LYP and CAM-B3LYP functionals. (d) Excited electron probability for the ground and excited state optimized structures.

experimental excitation energy is found when using the fully optimized B3LYP structure, which slightly underestimates the excitation energy, followed by the symmetry constrained CAM-

B3LYP structure, which overestimates the excitation energy. As such, full analysis was completed using the B3LYP fully optimized 32-unit structure and checked against the symmetry constrained CAM-B3LYP calculations. Calculations using range corrected functionals have recently been cited as reproducing experimental results more accurately in conjugated polymer, and it is therefore important to compare both types of functionals.[47] Analyses using the other methods and the geometries attained for each method are reported in the Supporting Information.

To investigate the extent of delocalization of the excited electron, we used the strategy of generating natural transition orbitals (NTOs)[48] for the lowest energy transition and then analyzing the excited state NTO's by orbital decomposition with a Mulliken partition scheme to assign an excited electron probability to atoms in the calculated structure.[49] NTOs describe the transition density matrix (TDM) in the molecular orbital basis and allow the presentation of the physically accurate TDM in the intuitive molecular orbital format. NTOs are generated from the canonical molecular orbitals using a transformation of the ground and excited orbitals as described by Martin.[48] Each NTO is associated with an eigenvalue $(\lambda_i)$ that acts as a coefficient that reflects the overall contribution of the orbital to the excitation. The population of these new orbitals can then be analyzed using population analysis techniques. Here we use the population partition of electrons into basis function $a$ in spin orbital $i$ suggested by Mulliken:

$$P_{i,a} = C_{a,i}^2 + \sum_{a \neq b} C_{a,i} C_{b,i} S_{a,b}$$

(3)

where $P_{i,a}$ is the population of basis function $a$ in single electron orbital $i$, $C$ is the atomic orbital coefficient matrix (assumed to be nonimaginary) and $S$ is the basis function overlap matrix. To attain the total probability for each atom in a particular NTO, all the basis function populations for an atom $N$ in orbital $i$ are summed together.

$$P_{N,i} = \sum_{a \in N} P_{i,a}$$

(4)

The total probability of finding an excited electron on an atom is assumed to be the sum of the population on that atom in each NTO, weighted by $\lambda_i$ for all $\lambda_i \geq 0.01$.

$$P_{N,e^-} = \sum_i \lambda_i P_{N,i}$$

(5)

To limit fast oscillations between neighboring atoms, the single atom probabilities are then summed to repeat thiophene units to give the electron probability per monomer unit $(P_n)$. All atoms except the four 'backbone' carbons and sulfur atom are excluded in this summation. This can be justified as >98% of the electron density in each NTO is supplied by the backbone atoms. When only the backbone atoms and a $\lambda_i \geq 0.01$ cutoff are used, more than 95% of the total single electron density for the transition is included. A plot of the excited electron probability vs monomer position is shown in Figure 4b for the $S_0$ to $S_1$ transition using both the fully optimized B3LYP and symmetry constrained CAM-B3LYP structures.

From the NTO analysis, the delocalization length $(L_e)$ of the excited electron was determined as the distance between the fewest contiguous thiophene units that sum to 95% of the total $e^-$ probability. For the B3LYP structure, this method gives an $L_e$ of 8.5 nm (22 repeat units) which corresponds to a 0.68

fraction of the total 32-unit oligomer length. Surprisingly, we find a very similar $L_e$ for the CAM-B3LYP symmetry constrained structure of 8.9 nm (23 repeat units) corresponding to a 0.72 fraction of the oligomer. Though the lowest CAM-B3LYP NTOs are less diffuse than the lowest B3LYP NTOs, many more NTOs are required to describe the excitation. The additional NTOs are however still fully delocalized and do not describe local excitations (see Supporting Information).[47] This suggests that CAM-B3LYP predicts an excitation that accesses more states in the conduction band than that described by B3LYP but that the band edge states, where thermalized particles are found, are more localized. In any case, we see that both methods support our spectroscopic measurements of substantial initial excitation volumes via intrachain delocalization.

While computational studies with large torsional defects (~90°) along the P3HT chain have shown that the electronic delocalization can be limited by torsional defects, this and other studies indicate that moderate torsional angles and chain curvature do not significantly limit the effective conjugation.[21] Even in the fully relaxed CAM-B3LYP geometry (see Supporting Information), it is found that $\pi$ and $\pi^*$ molecular orbitals describe different k-states within the same band with significant delocalization along the entire oligomer length, suggesting that torsional angles associated with ordered RR-P3HT domains should not act to limit the electron delocalization.

The relaxation of the excited state is known to act as a mechanism for increasing the exciton binding energy and it has been suggested that the exciton relaxation is associated with localization.[30] To investigate this phenomenon, $S_1$ excited state geometry optimizations of the oligothiophenes were performed. This model does not give temporal information about the relaxation of the excited state but shows the extent of localization of the electronic wave function in the relaxed excited state. For efficiency reasons, the 20-unit oligomer was studied and the starting structure for each excited state geometry optimization was the planar, symmetry constrained structure as the excited state favors a planar structure with an increased torsional potential when compared to the ground-state.[50,51]

To track geometry changes between the ground and excited state, the bond length alternation (BLA) between the double and single bonds in each thiophene unit was examined and is shown in Figure 4c. For both the B3LYP and CAM-B3LYP calculations, there is a change in BLA that is highest in the central part of the chain, with the CAM-B3LYP calculation showing a narrower area of large BLA change between the ground and excited states. This suggests that relaxed exciton calculated by CAM-B3LYP has a smaller delocalization than that calculated using B3LYP.

This effect is manifest in the NTO analysis by comparing the vertical excitation from the ground state optimized structure and the excited state optimized structure corresponding to the absorption and emission processes, respectively. The excited electron probability assigned to each monomer unit for absorption and emission using both the B3LYP and CAM-B3LYP functionals are shown in Figure 4d. For the ground state structure, the exciton length is similar for both CAM-B3LYP and B3LYP owing again to more NTOs being required to describe the CAM-B3LYP excitation. In the relaxed structure, the exciton length using B3LYP shows only very modest localization to the center of the chain while for CAM-

B3LYP the localization of the exciton is much more pronounced. This suggests that the thermalized exciton predicted by CAM-B3LYP is shorter than that predicted by B3LYP.

Our experimental and theoretical investigations of the intrinsic PL dynamics of thin film P3HT samples can be summarized as follows: primary excitations are initially delocalized along a substantial chain length (approaching 10 nm). The excitons sample a large volume in a partially bound state and subsequently relax on the subpicosecond time scale via both transfer to lower energy sites and structural localization along a polymer chain.

**PL and TA Dynamics in Polymer:Fullerene Blends.** We then turned our attention to blends with PCBM. The known benefit of thermal annealing in OPV devices derived from these materials[2−5,52] prompted us to also investigate the link between ultrafast PL dynamics and the morphological change induced by thermal annealing. Figure 5a shows the PL dynamics for the
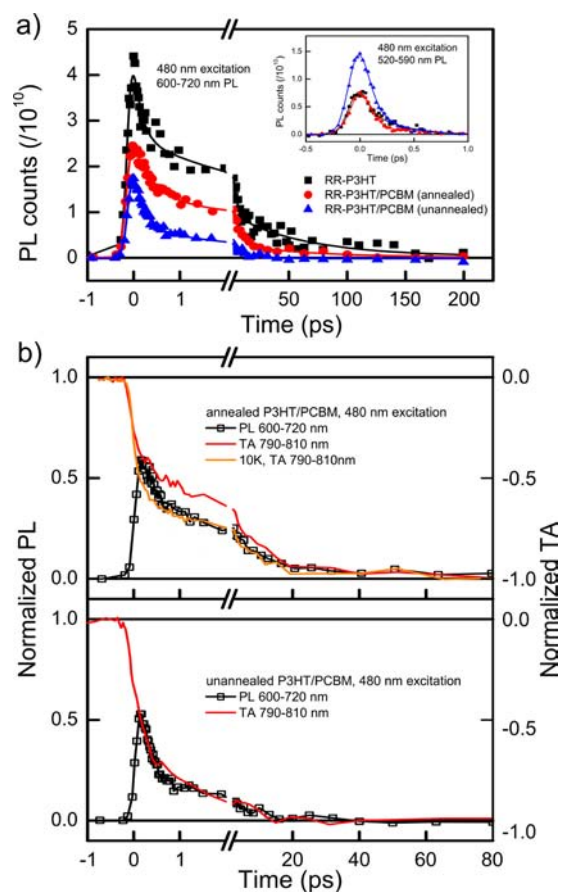


**Figure 5.** (a) PL decay kinetics for thin films of RR-P3HT and blends with PCBM following 480 nm excitation and probed in the low energy spectral range and the high energy range (inset). PL amplitudes are normalized on the basis of absorbed photons under identical measurement conditions. (b) Comparison of normalized PL decay kinetics and TA signal growth kinetics probed at 800 nm where hole polarons in P3HT absorb[2−4] for annealed (top) and unannealed (bottom) RR-P3HT/PCBM blend films following 480 nm excitation (7 $\mu$J/cm²). The TA dynamics are also shown for the annealed blend at 10 K. The PL is normalized based on the number of absorbed photons with reference to the unblended P3HT film in order to account for the static quenching component, while the TA signal is normalized to the peak photoinduced absorption signal.

P3HT/PCBM blends compared with neat P3HT for the high- and low-energy regions of the spectra. The ultrafast PL decay lifetime in the high-energy region (Figure 5a, inset) is virtually unaffected by the presence of PCBM, although the decay of this feature approaches our fastest time resolution in all samples. It is tempting to conclude that high energy excitons relax and transfer to lower energy sites more readily than being quenched via electron transfer to PCBM; however, as we discuss below, we cannot simply compare PL lifetimes without considering their amplitudes.

In all blends, the presence of PCBM shortens the exciton lifetime probed in the 600−720 nm window (Figure 5a). This observation, quantified by the fitted lifetimes in Table 1,

**Table 1. Fitting Parameters for PL Decay in Films of P3HT and Blends with PCBM after 480 nm Excitation**

| | P3HT | unannealed blend | annealed blend |
|---|---|---|---|
| $\tau_1\ (A_1)^a$ | 110 fs | 90 fs | 220 fs |
| | (0.35) | (0.18) | (0.29) |
| $\tau_2\ (A_2)^a$ | 1.2 ps | 310 fs | 1.6 ps |
| | (0.43) | (0.29) | (0.16) |
| $\tau_3\ (A_3)^a$ | 39 ps | 7.7 ps | 26 ps |
| | (0.22) | (0.06) | (0.12) |
| Dynamic quenching[b] | - | 0.87 | 0.33 |
| Static quenching[c] | - | 0.47 | 0.41 |
| Total time-resolved quenching[d] | - | 0.93 | 0.62 |
| Time integrated quenching[e] | - | 0.91 | 0.80 |

[a]Amplitudes for P3HT normalized to 1, and amplitudes for blends normalized based on absolute intensities per absorbed photon in P3HT measurement under the same conditions. [b]Dynamic quenching assessed by renormalizing all amplitudes to sum to 1 for blends and calculating $\{[\sum A_i \tau_i\ (\text{P3HT})] - [\sum A_i \tau_i\ (\text{blend})]\}/[\sum A_i \tau_i\ (\text{P3HT})]$. [c]Static quenching assessed by calculating $((\sum A_i\ (\text{P3HT}) - (\sum A_i\ (\text{blend}))/(\sum A_i\ (\text{P3HT}))$. [d]Total time-resolved quenching (dynamic + static) assessed using amplitudes given (without renormalizing) and calculating $\{[\sum A_i \tau_i\ (\text{P3HT})] - [\sum A_i \tau_i\ (\text{blend})]\}/[\sum A_i \tau_i\ (\text{P3HT})]$. [e]Time integrated intensities refer to measurements taken with the Kerr shutter open.

appears consistent with standard models presented for charge generation via bound excitons in OPVs.[53] When comparing the dynamics for annealed and unannealed blends, we see that the dominant ~1 ps decay component for the annealed blend is shortened to ~200 fs for the unannealed blend, consistent with previous transient absorption (TA) spectroscopy studies that attribute the shortening to diffusion in a more finely phase separated blend.[2−4]

By summing the decay constants weighted by their relative amplitudes, we can quantify the total amount of exciton quenching that is resolved by the shortened lifetimes of a given blend (i.e., the *dynamic quenching*). We find that dynamic quenching can only account for 87% and 33% of the exciton population decay in the case of unannealed and annealed blends, respectively. These values are too low to account for the high quantum efficiencies of photocurrent generation in these P3HT:PCBM blends (~70% external quantum efficiency, see Supporting Information), prompting us to look more closely at total time-integrated quenching and variation in PL amplitudes.

Here, we exploit the ability of our system to maintain the same detection efficiency upon changing samples with all other components fixed, in addition to the ability to switch to time-

integrated mode under the same excitation conditions simply by removing a polarizer from the Kerr Shutter and blocking the gate beam. In all comparisons between samples, we ensure that the excitation wavelength and intensity is fixed and we subsequently correct PL intensities according to the small variations in optical density (typically less than 10% variation for samples compared). The time-integrated PL quenching efficiency is readily obtained by comparing time- and wavelength integrated PL intensities for blends and unblended P3HT films. The analysis summarized in Table 1 reveals high levels of PL quenching of 91% and 80% for the unannealed and annealed blends, respectively. Having established quenching levels that are consistent with previous measurements,[2−4] we were able to attribute significance to the strong variation observed in the initial PL amplitudes for the same excitation densities and detection configuration for each sample. Figure 5a reveals that the initial PL amplitude at 600−720 nm is reduced by 47% and 41% in the unannealed and annealed blends, respectively. When considering the degree to which this static quenching channel depletes the population of photoexcitations before dynamic quenching takes effect (Table 1), we can quantitatively account for all of the observed time-integrated PL quenching with our time-resolved parameters in the case of the unannealed blend and most of the time-integrated PL for the annealed blend. The residual 18% quenching that is not accounted for by the static and dynamic quenching parameters we resolve in the annealed blend is probably due to quenching of the PL tail on longer time scales that are not well resolved in this measurement. By directly resolving nearly all of the PL quenching, we confirm that our failure to directly resolve a ~500 ps decay component in the unblended film is relatively inconsequential. On the contrary, if we had resolved substantial dynamic quenching from a 500-ps decay, we may incorrectly believe that we had accounted for all of the quenching and not looked more closely at the amplitudes.

Our measurement of static quenching must be considered a lower bound because the unblended P3HT film we reference to does not account for disorder induced by PCBM, which would increase the polymers PL intensity before considering quenching by electron transfer. To illustrate this point, we measured P3HT blended with triptycene, a molecule lacking the driving force to participate in electron transfer, but whose comparable dimensionality to PCBM induces disorder in polymer blends.[54] As shown in the Supporting Information, triptycene addition increases the PL amplitude, particularly for high energy emission associated with disordered polymer chains. This effect also accounts for the *increased* initial amplitude of high-energy emission for the unannealed PCBM blend (Figure 5a, inset) compared with unblended P3HT. The possibility of static quenching via defects (e.g., charges) in the unblended reference sample would also reduce the PL amplitude of the unblended film and therefore cause under-estimation of static quenching in the blend.

We are able to confirm that the observed PL quenching is directly attributed to charge generation by comparing our PL decay to transient absorption (TA) dynamics of charge formation for the same samples. Figure 5b shows the growth in charge absorption (probed at 800 nm, where the TA spectrum of excitons exhibits an isosbestic point and charges absorb)[2−4] and the PL decay for both films. We find that growth in charge absorption (i.e., negative $\Delta T/T$) corresponds very closely to the PL decay integrated over the main peak. Moreover, the correspondence is only achieved when including

the large static quenching component in the PL intensity normalization, which matches very closely with the prompt charge photogeneration component resolved via TA spectroscopy.

The observation that nearly half of the emissive population is lost within the time response of our measurement highlights the role of charge photogeneration from hot primary excitations. Following the same arguments applied to static quenching via annihilation (vide supra), the appearance of static quenching requires an actual quenching time constant of shorter than 60 fs convoluted with our instrument response function. This is strong evidence that a large fraction of charge photogeneration happens on a time scale competitive with that we measured for the formation of relaxed excitons. Beyond the static quenching component, we see that over 70% of all charges generated are already present within ~500 fs for the unannealed blend and 1 ps for the annealed blend. The high yield of charge photogeneration on this time scale is significant when considering the characteristics of excitations we found for unblended P3HT films on a subpicosecond time scale; most charges are formed when excitations are very delocalized, highly mobile, and not yet structurally relaxed. As previously speculated by Marsh et al.,[4] we find that these attributes can account for the high yields of ultrafast of charge photogeneration in phase separated blends that cannot be explained by relatively slow exciton diffusion constants measured on longer time scales.

Another confirmation that charge photogeneration occurs largely from hot excitations is found when undertaking TA spectroscopy at low temperature. Consistent with measurements from Grzegorczyk et al.,[55] the charge photogeneration dynamics at 10 K in the annealed blend are virtually unchanged from room temperature (Figure 5b, top panel). The temperature invariance suggests that charge photogeneration largely circumvents structural relaxation, which would otherwise impede excitations from reaching a heterojunction at low temperature. Referring to the temperature dependent exciton diffusion studies of Mikhnenko et al.,[38] we see that the temperature independent initial downhill phase of exciton motion is most relevant to charge photogeneration in blends. If anything, the 10 K charge photogeneration kinetics suggest a slightly higher degree of prompt charge generation, which may result from a longer coherence length in the initial excitation.

**Free Charge Carrier Generation.** Next, we consider the implications of our findings on the process of free carrier generation. We followed the analysis presented by Howard et al. to determine the branching ratio between free and bound charges for these samples by resolving the density dependence of charge recombination via TA spectroscopy on ns-$\mu$s time scales and globally fitting to a kinetic model.[3] This analysis, shown in the Supporting Information, results in 77% and 54% of the total charge population being free for the annealed and unannealed blends, respectively, consistent with the values previously published.[3] We see that the yield of free charge generation in the annealed blend is similar to the yield of charges formed on an ultrafast time scale (~500 fs) competitive with relaxation. While an even higher charge yield is found for the unannealed blend on an ultrafast time scale, the lack of extended polymer domains in that blend prevents charge photogeneration over a sufficient length scale to create free charges, even if charge generation occurs rapidly.[2−4]

Recent studies have highlighted the key role of short-lived delocalized charge states in promoting the formation of charge

pairs that are sufficiently spaced to avoid subsequent collapse to Coulombically bound charge-transfer states.[10,11] In demonstrating that the initial polymer-based excitations have a remarkably large volume (due to their length), and that a significant fraction is quenched by PCBM prior to exciton localization, our results suggest that the crucial delocalized charge states may inherit their delocalization by coupling directly to the initial polymer excitation. As depicted in Scheme 1, the large volume of hot excitons presents a fleeting opportunity to create free charge carriers by quenching over significant distances from a nonrelaxed state.

**Scheme 1. Proposed Model for Free Charge Photogeneration via Coupling between Delocalized Excitons and Delocalized Interfacial Charge Transfer States**
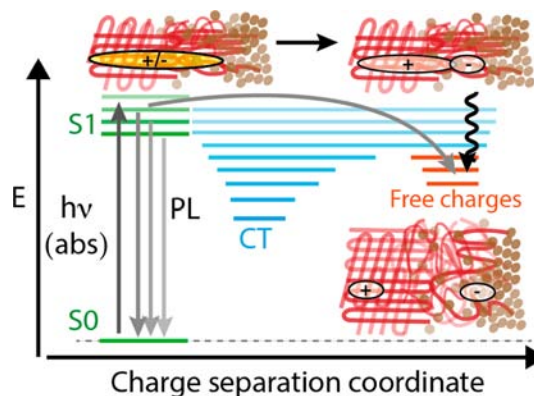


The idea that free charge carriers are preferentially generated from delocalized primary excitations implies that free charges are preferentially formed on an ultrafast time scale following optical excitation. Indeed, high yields of free charge photogeneration have recently been measured on ultrafast time scales via TA spectroscopy at terahertz probe wavelengths where free charge carrier dynamics are isolated.[5,6]

A further implication of this model is that charge photogeneration is expected be more effective when charge pairs are formed along the direction of the polymer chains, thereby benefitting from intrachain delocalization of the primary excitation. Again, this appears consistent with several observations from previous work; considering a blend with high photocurrent quantum efficiency, polymer chains in annealed P3HT:PCBM blend films arrange in extended chains, forming semicrystalline lamellae separated by PCBM phases.[56] On the other hand, blends with low efficiency (e.g., unannealed P3HT:PCBM blends, or polymer:polymer blends) are often characterized by bound charge pairs formed orthogonally to the polymer chains.[57,58] Identifying the preferred orientation of donor/acceptor interactions creates opportunities to develop new materials that feature well-defined extended chains suitable for supporting delocalized excitations and coupling to electron acceptors at the ends. In one recent example, Johnson et al. showed that P3HT chains of 18 monomer units length were entirely quenched by a terminal benzathiadiazole acceptor as fast as 40 fs, depending on how strongly coupled the polymer chain and the acceptor are.[59]

Finally, we note that delocalized hot excitons may also be relevant to observations of direct charge photogeneration in neat polymer films. Free charge photogeneration yields have are found to depend on film morphology (e.g., from different casting solvents).[8,9] On the one hand, the observation that

charges are formed on an ultrafast time scale has led to this morphological effect being ascribed to different interchain coupling strengths.[8] On the other hand, delayed PL measurements of charge recombination point to an extrinsic mechanism where charge pairs are formed at morphological interfaces between ordered and disordered polymer regions with slightly offset orbital energies.[9] These models can be reconciled if delocalized hot excitons were formed across morphological interfaces and rapidly relax to form interfacial charge pairs, thus satisfying the observations that charge pairs are localized at interfaces, yet their ultrafast formation is not preceded by diffusion. The proposed model is also consistent with single molecule PL investigations of quenching morphological defects. By undertaking time-resolved single molecule PL spectroscopy and quantitatively accounting for all absorbed and emitted photons, Lin et al. showed that polymer chains exhibiting lower PL quantum yields did not have shorter PL lifetimes, therefore differences were attributed to lower initial PL amplitudes as a result of 'dark' regions.[60] Here, we suggest that the dark regions correspond to configurations where delocalized hot excitons interact with conformational defects and lead to the appearance of static quenching like we observe in polymer:fullerene blend films and in neat polymer films at high excitation density.

## CONCLUSIONS

By applying broadband ultrafast PL spectroscopy to thin films of P3HT and fullerene blends, we resolve the nature of the excitons on the subpicosecond time scale that dominates charge photogeneration in OPVs. We capture high-energy emission from nonrelaxed excitons followed by rapid energetic relaxation on a logarithmic time scale. By resolving ultrafast annihilation at high excitation density and applying a Perrin-type quenching model, we measure an initial excitation volume approaching 20 nm$^3$. Consistent with quantum chemical calculations, our measurement reflects an initial excitation that is substantially delocalized along a polymer chain prior to localization induced by structural relaxation. The time-dependence of annihilation also shows that excitons are highly mobile on a time scale competitive with structural relaxation, with the reduction in mobility correlated to energetic relaxation. In fullerene blends, we observe substantial quenching of the ultrafast PL amplitudes (i.e., faster than our instrument limit), with subpicosecond quenching accounting for most of the rest of the total quenching. Time-resolved PL measurements correlate well with TA spectroscopy measurements of the same samples, confirming that the emissive population is a good probe of the total population. We find that properties that we measure for excitons on subpicosecond time scales have a pronounced effect on charge photogeneration. The large volume and high mobility of nonrelaxed excitons account for the charge photogeneration being substantially faster than predicted via simple exciton diffusion, as well as being independent of temperature. Moreover, we suggest that highly delocalized intrachain excitons may couple to highly delocalized charge transfer states along the direction of the chain to preferentially form charge pairs that are well separated upon subsequent thermalization. Our model appears consistent with numerous other observations of free charge photogeneration, including its morphological dependence. This should motivate the design of new materials that exploit ultrafast exciton delocalization by engineering charge separating interfaces at the ends of extended polymer chains. We expect that the techniques we have introduced for interrogating the properties of initial excitations

will provide a powerful means of examining the suitability of new OPV materials.

## ASSOCIATED CONTENT

**S** Supporting Information

Ultrafast PL spectra for RR-P3HT with 570 nm excitation, ultrafast PL spectra for RRa-P3HT, derivation of the modified Perrin equation, ultrafast PL anisotropy, further details about quantum chemical calculations, spectrally resolved photocurrent for a complete device and corresponding ultrafast PL data, ultrafast PL spectra for a P3HT:triptycene (TPC) blend film, TA intensity dependent charge recombination with corresponding fitting details. This material is available free of charge via the Internet at http://pubs.acs.org.

## AUTHOR INFORMATION

**Corresponding Author**

Justin.Hodgkiss@vuw.ac.nz.

**Notes**

The authors declare no competing financial interest.

## ACKNOWLEDGMENTS

## REFERENCES

(1) Shaw, P. E.; Ruseckas, A.; Samuel, I. D. W. *Adv. Mater.* **2008**, *20*, 3516−3520.

(2) Guo, J.; Ohkita, H.; Benten, H.; Ito, S. *J. Am. Chem. Soc.* **2013**, *132*, 6154−6164.

(3) Howard, I. A.; Mauer, R.; Meister, M.; Laquai, F. *J. Am. Chem. Soc.* **2010**, *132*, 14866−14876.

(4) Marsh, R. A.; Hodgkiss, J. M.; Albert-Seifried, S.; Friend, R. H. *Nano Lett.* **2010**, *10*, 923−930.

(5) Piris, J.; Dykstra, T. E.; Bakulin, A. A.; Loosdrecht, P. H. M. V.; Knulst, W.; Trinh, M. T.; Schins, J. M.; Siebbeles, L. D. A. *J. Phys. Chem. C* **2009**, *113*, 14500−14506.

(6) Cooke, D. G.; Krebs, F. C.; Jepsen, P. U. *Phys. Rev. Lett.* **2012**, *108*, 056603.

(7) Grancini, G.; Maiuri, M.; Fazzi, D.; Petrozza, A.; Egelhaaf, H.-J.; Brida, D.; Cerullo, G.; Lanzani, G. *Nat. Mater.* **2013**, *11*, 29−33.

(8) Sheng, C. X.; Tong, M.; Singh, S.; Vardeny, Z. *Phys. Rev. B* **2007**, *75*, 085206.

(9) Paquin, F.; Latini, G.; Sakowicz, M.; Karsenti, P.-L.; Wang, L.; Beljonne, D.; Stingelin, N.; Silva, C. *Phys. Rev. Lett.* **2011**, *106*, 197401−197404.

(10) Bakulin, A. A.; Rao, A.; Pavelyev, V. G.; van Loosdrecht, P. H. M.; Pshenichnikov, M. S.; Niedzialek, D.; Cornil, J.; Beljonne, D.; Friend, R. H. *Science* **2012**, *335*, 1340−1344.

(11) Jailaubekov, A. E.; Willard, A. P.; Tritsch, J. R.; Chan, W.-L.; Sai, N.; Gearba, R.; Kaake, L. G.; Williams, K. J.; Leung, K.; Rossky, P. J.; Zhu, X.-Y. *Nat. Mater.* **2013**, *12*, 66−73.

(12) Brédas, J.-L.; Norton, J. E.; Cornil, J.; Coropceanu, V. *Acc. Chem. Res.* **2009**, *42*, 1691−1699.

(13) Scheblykin, I. G.; Yartsev, A.; Pullerits, T.; Gulbinas, V.; Sundström, V. *J Phys Chem B* **2007**, *111*, 6303−6321.

(14) Ruseckas, A.; Wood, P.; Samuel, I.; Webster, G.; Mitchell, W.; Burn, P.; Sundström, V. *Phys. Rev. B* **2005**, *72*, 115214.

(15) Chang, M.; Frampton, M.; Anderson, H.; Herz, L. *Phys. Rev. Lett.* **2007**, *98*, 027402.

(16) Chang, M.-H.; Hoffmann, M.; Anderson, H. L.; Herz, L. M. *J. Am. Chem. Soc.* **2008**, *130*, 10171−10178.

(17) Collini, E.; Scholes, G. D. *Science* **2009**, *323*, 369−373.

(18) Banerji, N.; Cowan, S.; Leclerc, M.; Vauthey, E.; Heeger, A. J. *J. Am. Chem. Soc.* **2010**, *132*, 17459−17470.

(19) Banerji, N.; Cowan, S.; Vauthey, E.; Heeger, A. J. *J. Phys. Chem. C* **2011**, *115*, 9726−9739.

(20) Banerji, N. *J. Mater. Chem. C* **2013**, *1*, 3052.

(21) Beenken, W. J. D. *Phys. Status Solidi A* **2009**, 2750−2756.

(22) Barford, W. *J. Phys. Chem. A* **2013**, *117*, 2665−2671.

(23) Kaake, L. G.; Moses, D.; Heeger, A. J. *J. Phys. Chem. Lett.* **2013**, *4*, 2264−2268.

(24) Thakur, A. K.; Wantz, G.; Garcia-Belmonte, G.; Bisquert, J.; Hirsch, L. *Sol. Energy Mater. Sol. Cells* **2011**, *95*, 2131−2135.

(25) Schmidt, B.; Laimgruber, S.; Zinth, W.; Gilch, P. *Appl. Phys. B: Lasers Opt.* **2003**, *76*, 809−814.

(26) Nakamura, R.; Kanematsu, Y. *Rev. Sci. Instrum.* **2004**, *75*, 636−639.

(27) Arzhantsev, S.; Maroncelli, M. *Appl. Spectrosc.* **2005**, *59*, 206−220.

(28) Frisch, M.; Trucks, G. W.; Schlegel, H. B.; Scuseria, G. E.; Robb, M. A.; Cheeseman, J. R.; Scalmani, G.; Barone, V.; Mennucci, B.; Petersson, G. A.et al.*Gaussian 09*Gaussian, Inc.: Wallingford, CT, 2009.

(29) Yanai, T.; Tew, D. P.; Handy, N. C. *Chem. Phys. Lett.* **2004**, *393*, 51−57.

(30) Nayyar, I. H.; Batista, E. R.; Tretiak, S.; Saxena, A.; Smith, D. L.; Martin, R. L. *J. Phys. Chem. Lett.* **2011**, *2*, 566−571.

(31) Reish, M. E.; Nam, S.; Lee, W.; Woo, H. Y.; Gordon, K. C. *J. Phys. Chem. C* **2012**, *116*, 21255−21266.

(32) Lu, T.; Chen, F. *J. Comput. Chem.* **2012**, *33*, 580−592.

(33) Xie, Y.; Li, Y.; Xiao, L.; Qiao, Q.; Dhakal, R.; Zhang, Z.; Gong, Q.; Galipeau, D.; Yan, X. *J. Phys. Chem. C* **2010**, *114*, 14590−14600.

(34) Trotzky, S.; Hoyer, T.; Tuszynski, W.; Lienau, C.; Parisi, J. *J. Phys. D: Appl. Phys.* **2009**, *42*, 055105.

(35) Cook, S.; Liyuan, H.; Furube, A.; Katoh, R. *J. Phys. Chem. C* **2010**, *114*, 10962−10968.

(36) Kersting, R.; Lemmer, U.; Mahrt, R. F.; Leo, K.; Kurz, H.; Bässler, H.; Göbel, E. O. *Phys. Rev. Lett.* **1993**, *70*, 3820−3823.

(37) Hayes, G. R.; Samuel, I.; Phillips, R. T. *Phys. Rev. B* **1995**, *52*, R11569−R11572.

(38) Mikhnenko, O. V.; Cordella, F.; Sieval, A. B.; Hummelen, J. C.; Blom, P. W. M.; Loi, M. A. *J. Phys. Chem. B* **2008**, *112*, 11601−11604.

(39) Yu, W.; Zhou, J.; Bragg, A. E. *J. Phys. Chem. Lett.* **2012**, *3*, 1321−1328.

(40) Perrin, F. *C. R. Hebd. Seances Acad. Sci.* **1924**, *178*, 1978.

(41) Guo, J.; Ohkita, H.; Benten, H.; Ito, S. *J. Am. Chem. Soc.* **2009**, *131*, 16869−16880.

(42) Dogariu, A.; Vacar, D.; Heeger, A. *Phys. Rev. B* **1998**, *58*, 10218−10224.

(43) Albert-Seifried, S.; Friend, R. H. *Appl. Phys. Lett.* **2011**, *98*, 223304.

(44) Kersting, R.; Mollay, B.; Rusch, M.; Wenisch, J.; Leising, G.; Kauffmann, H. F. *J. Chem. Phys.* **1997**, *106*, 2850−2864.

(45) Yamagata, H.; Spano, F. C. *J. Chem. Phys.* **2012**, *136*, 184901.

(46) Brinkmann, M. *J. Polym. Sci. B: Polym. Phys.* **2011**, *49*, 1218−1233.

(47) Pandey, L.; Doiron, C.; Sears, J. S.; Brédas, J.-L. *Phys. Chem. Chem. Phys.* **2012**, *14*, 14243.

(48) Martin, R. L. *J. Chem. Phys.* **2003**, *118*, 4775−4777.

(49) Bjorgaard, J. A.; Köse, M. E. *J. Phys. Chem. A* **2013**, *117*, 3869−3876.

(50) Tretiak, S.; Saxena, A.; Martin, R. L.; Bishop, A. R. *Phys. Rev. Lett.* **2002**, *89*, 097402 EP −.

(51) Clark, J.; Nelson, T.; Tretiak, S.; Cirmi, G.; Lanzani, G. *Nat. Phys.* **2012**, *8*, 225−231.

(52) Ma, W.; Yang, C.; Gong, X.; Lee, K.; Heeger, A. J. *Adv. Funct. Mater.* **2005**, *15*, 1617−1622.

(53) Coakley, K. M.; McGehee, M. D. *Chem. Mater.* **2004**, *16*, 4533−4542.

(54) Lomas, C. R.; Hodgkiss, J. M. *Supramol. Chem.* **2013**, *24*, 526−531.

(55) Grzegorczyk, W. J.; Savenije, T. J.; Dykstra, T. E.; Piris, J.; Schins, J. M.; Siebbeles, L. D. A. *J. Phys. Chem. C* **2010**, *114*, 5182−5186.

(56) Kohn, P.; Rong, Z.; Scherer, K. H.; Sepe, A.; Sommer, M.; Müller-Buschbaum, P.; Friend, R. H.; Steiner, U.; Hüttner, S. *Macromolecules* **2013**, *46*, 4002−4013.

(57) Huang, Y.-S.; Westenhoff, S.; Avilov, I.; Sreearunothai, P.; Hodgkiss, J. M.; Deleener, C.; Friend, R. H.; Beljonne, D. *Nat. Mater.* **2008**, *7*, 483−489.

(58) Hodgkiss, J. M.; Campbell, A. R.; Marsh, R. A.; Rao, A.; Albert-Seifried, S.; Friend, R. H. *Phys. Rev. Lett.* **2010**, *104*, 177701.

(59) Johnson, K.; Huang, Y.-S.; Huettner, S.; Sommer, M.; Brinkmann, M.; Mulherin, R.; Niedzialek, D.; Beljonne, D.; Clark, J.; Huck, W. T. S.; Friend, R. H. *J. Am. Chem. Soc.* **2013**, *135*, 5074−5083.

(60) Lin, H.; Tian, Y.; Zapadka, K.; Persson, G.; Thomsson, D.; Mirzov, O.; Larsson, P.-O.; Widengren, J.; Scheblykin, I. G. *Nano Lett.* **2009**, *9*, 4456−4461.